

Published in final edited form as:

Magn Reson Med. 2014 August ; 72(2): 362–368. doi:10.1002/mrm.24926.

Absolute Oxygen R_{1e} Imaging *In Vivo* with Pulse Electron Paramagnetic Resonance

Boris Epel¹, Michael K. Bowman², Colin Mailer¹, and Howard J. Halpern¹

¹Center for EPR Imaging *In Vivo* Physiology, The University of Chicago, Department of Radiation and Cellular Oncology (MC 1105), Chicago, Illinois 60637

²Department of Chemistry, The University of Alabama, Tuscaloosa, AL 35487

Abstract

Purpose—Tissue oxygen (O_2) levels are among the most important and most quantifiable stimuli to which cells and tissues respond through inducible signaling pathways. Tumor O_2 levels are major determinants of the response to cancer therapy. Developing more accurate measurements and images of tissue O_2 partial pressure (pO_2), assumes enormous practical, biological, and medical importance.

Methods—We present a fundamentally new technique to image pO_2 in tumors and tissues with pulse electron paramagnetic resonance (EPR) imaging enabled by an injected, nontoxic, triaryl methyl (trityl) spin probe whose unpaired electron's slow relaxation rates report the tissue pO_2 . Heretofore, virtually all *in vivo* EPR O_2 imaging measures pO_2 with the transverse electron spin relaxation rate, R_{2e} , which is susceptible to the self-relaxation confounding O_2 sensitivity.

Results—We found that the trityl electron longitudinal relaxation rate, R_{1e} , is an order of magnitude less sensitive to confounding self-relaxation. R_{1e} imaging has greater accuracy and brings EPR O_2 images to an absolute pO_2 image, within uncertainties.

Conclusion— R_{1e} imaging more accurately determines oxygenation of cancer and normal tissue in animal models than has been available. It will enable enhanced, rapid, noninvasive O_2 images for understanding oxygen biology and the relationship of oxygenation patterns to therapy outcome in living animal systems.

Keywords

Oxygen; Imaging; EPR; Pulse; R_1 ; Spin Lattice Relaxation; *In Vivo*; Tumor

Introduction

Importance of EPR O_2 Images

Molecular oxygen, O_2 , is a crucial molecular determinant of states of human health and disease. One third of human deaths are due to diseases of O_2 deprivation such as ischemic

Corresponding author: Prof. Howard Halpern, M.D., Ph.D Center for EPR Imaging in Vivo Physiology, University of Chicago, Department of Radiation and Cellular Oncology, MC1105, Rm: ESB-05, 5841 S. Maryland Avenue, Chicago, IL 60637, USA. h-halpern@uchicago.edu; Tel. +1(773)702-6871; Fax: +1(773)702-5940.

heart disease and cerebrovascular disease (1). Regions of low O_2 , hypoxia, thought to be a universal characteristic of solid tumors, (2) reduce the efficacy of radiation therapy in their treatment (3). The importance of organismal response to hypoxia is reflected in the hundreds of genes regulated by hypoxia inducible factor-1 (HIF-1). (4,5) As will be seen in animal model tumor images presented in this paper, large pO_2 gradients separate regions of high and low pO_2 throughout a tumor. *In vivo* quantification of tissue pO_2 in disease states, thus, requires imaging to fully characterize the oxygenation state of the entire tumor. EPR O_2 images may define the mechanism by which hypoxia creates resistance to radiation, which remains elusive. (2) pO_2 EPR images registered with either stereotactic biopsies or gene induction images can define quantitative gene induction response to local pO_2 - *in vivo* - in states of health and disease (6).

R_1 images solve confounding self-relaxation of O_2 EPR Images

Heretofore, in *in vivo* EPR O_2 images, pO_2 has been measured via the broadening of the EPR spectral lines of an injected spin probe predominantly through Heisenberg spin exchange (HSE) with local O_2 . (7) The spin probe is a paramagnetic trityl molecule (8) with a single narrow EPR line whose relaxation times are long enough to enable pulse imaging. Spin packet spectral line width (LW) broadening in a continuous wave (CW) experiment is physically equivalent to increasing the transverse magnetization relaxation rate (R_{2e}) in a pulse experiment. $LW = (\gamma_e T_{2e})^{-1} = R_{2e} / \gamma_e$; $\gamma_e \equiv$ gyromagnetic ratio of the electron (9). Both R_{2e} and R_{1e} depend linearly on pO_2 (8,10,11). The spin probe collision rate with extremely rapidly relaxing O_2 , increases R_{2e} , destroying the magnetization phase coherence. EPR images of R_{2e} yielded quantitative O_2 images *in vivo* (12–15) providing about 1 mm resolution, and a method less susceptible to confounding biologic variation than other techniques (2).

HSE between the unpaired electrons of O_2 and spin probe similarly increases the spin probe electron spin-lattice or longitudinal relaxation rate R_{1e} , which measures the loss of the trityl spin magnetization energy to the lattice, predominantly to the O_2 (7). However, HSE self-relaxation processes, HSE interactions between spin probes, affect R_{1e} and R_{2e} differently. HSE between two trityl molecules with differing EPR frequencies produces additional precession phase shifts that increase the R_{2e} (7). HSE does not alter the total energy of an interacting spin probe pair, and therefore does not affect the electron spin system energy - the longitudinal magnetization. Use of image pulse sequences dependent on R_{1e} reduces probe self-relaxation by nearly an order of magnitude. At this level, essentially the only physiologic R_{1e} relaxation rate increase is due to O_2 .

Imaging of trityl concentration is difficult

Trityl concentration, referred to as [trityl], is related to the amplitude of the trityl signal in each voxel and might be useful to correct the effect of [trityl] self-relaxation on R_{2e} . However the accuracy in determining [trityl], using local signal amplitude is complicated by the extracellular fluid compartment distribution of trityl (16) and the variability of the extracellular volume fraction in the chaotic tumor environment. Trityl distribution volume varies from voxel to voxel making [trityl] correction difficult, blurring R_{2e} -based pO_2

accuracy. We find, here, R_{1e} pO₂ images are far less [trityl] dependent and more accurate than R_{2e} -based images.

Imaging longitudinal relaxation rate R_{1e} is straightforward and accurate with pulse EPR

In saline solutions and very low [trityl], R_{1e} is close to R_{2e} at physiologic temperatures. Although quantitative oxygen R_{1e} EPR measurements (11,17) and images (18) have been reported these were continuous wave studies. Pulse imaging is more efficient, shows better precision and, as we will show in this paper, accuracy. (19) This work is the first to demonstrate direct, quantitative, pulse *in vivo* R_{1e} images. The long electron relaxation times of the trityl OX063 (8) with T_{1e} and T_{2e} of $\sim 7 \mu\text{s}$ at hypoxic conditions, and consequent slow relaxation rates enable pulse R_{1e} images with current RF technology. We read out R_{1e} from each voxel using inversion recovery (IR) (20), imaging the recovering longitudinal magnetization as a function of time after the inversion pulse using electron spin echo (ESE) imaging (14,21) - a tomographic frequency-encoding method. We thus refer to inversion recovery with ESE readout as IRESE.

The inversion recovery sequence IRESE (Fig. 1), inverts the spin polarization with a π -pulse preceding the ESE $\pi/2$ - π detection sequence. The recovery is measured as a function of the delay T (Fig. 2) between the inversion pulse and the ESE detection sequence. The coefficient A in the equation in Fig. 2 is less than or equal to, but near, two. Values less than 2 account for incomplete EPR line inversion. A single echo time τ is fixed at an optimum slightly longer than the imager dead time.

This study compares R_{1e} with R_{2e} imaging using a 250 MHz pulse imager (14). We demonstrate that *in vivo* R_{1e} imaging shows much higher absolute pO₂ accuracy, overcoming the limitations imposed by [trityl] relaxation on R_{2e} imaging.

Methods

Imaging Methods

A pulse 250 MHz imager (14) was enhanced with a passive transmit-receive switch (22) and $\pi/2$ - and π - pulses of equal duration/bandwidth (23). The imager was controlled with SpecMan4EPR v. 1.1.6 (24).

Image acquisition time and spatial resolution were fixed at, respectively, 10 minutes and 1.5 mm. Spatial resolution of the ESE and IRESE images were defined by the Rayleigh resolution criterion (14,25). We used the same pulse sequences for phantoms and for animal imaging. The standard deviation of the relaxation times/rates in homogeneous phantoms, excluding two outer layers to avoid partial volume artifacts, was used as an estimation of relaxation time/rate errors. Tables 1 and 2 present parameters of the R_{1e} and R_{2e} sequences. The repetition time, T_R , for ESE sequences was adjusted to keep constant the delay between the last pulse in a sequence and the first pulse of the next sequence. For accurate R_{1e} in IRESE images the image recorded at infinite recovery time T was equated to an image recorded without an inversion pulse. For voxel intensity fitting to an exponential recovery function, a T equal to $36 \mu\text{s}$ was assigned to this image.

For images, (14,26) 208 equal solid angle projections (27) were acquired; gradient $|\vec{G}|=15$ mT/m; field of view =4.24 cm. A 53 baseline projections obtained with 1.5 mT lower main field were acquired with every fourth projection and subtracted from the previous four projections. Projection numbers were expanded with four-fold cubic B-spline interpolation (27) and were filtered with a 3D Ram-Lak filter cutoff at one half the Nyquist frequency. Voxels with amplitude less than 15% maximum at the shortest delay were eliminated (thresholded). (14).

The system frequency band-pass function for each acquisition technique was measured using zero gradient sample signal amplitude at 50 spanning B_0 fields (14). Projections were normalized using this function. Image analysis was performed with in-house software written using MATLAB (Mathworks, Inc., Natick, MA).

The spatial resolution of an image can be quantified by the response of an image to an abrupt step function change in sample density fitted with the Gauss error function ($\text{erf}(x/2\sigma)$). The width of this error function $\sigma=1.5\text{mm}$ is an estimate of the ESE image spatial resolution. IRESE image has the same spatial resolution.

Spin Probe

Spin probe was the trityl OX063 radical methyl-tris[8-carboxy-2,2,6,6-tetrakis[2-hydroxyethyl]benzo[1,2-d:4,5-d']bis[1,3]dithiol-4-yl]-trisodium salt, GE Healthcare (LittleChalfont, Buckinghamshire, UK). Phantoms with 1 mM spin probe in saline were glass cylinders 9.5 mm i.d., 45 mm long. The 0% O_2 sample was degassed *via* freeze-pump-thaw; the 9.3% O_2 sample was bubbled with a 9.3%:90.7% oxygen-nitrogen mixture and epoxy sealed. For measuring oxygen concentration dependence, the phantoms were bubbled *in situ* with humidified gas mixture. 30 minutes or more were given for oxygen equilibration during these measurements.

Non-imaging vs. imaging conditions

Acquisition of spatial information requires considerable time, which, for *in vivo* imaging, is limited by the animal physiology. Therefore imaging protocols have to balance the precision of the measurements with the experiment's duration. As a result, the relaxation times in imaging protocols are estimated from only five points (R_{2e}) or eight points (R_{1e}) on the decay curve. Such restrictions do not apply for non-imaging measurements on phantoms, which have larger numbers of delays (T) from the inversion pulse (80 vs 5 R_{2e} – 8 R_{1e} for imaging) and wider T_R interval (at least 5 hypoxic T_{1e} for non-imaging vs $\sim T_{1e}$ for imaging). Non-imaging measurements were repeated ~ 50 times, 20 seconds for each measurement; data were fitted independently, and the average was presented.

Animal Imaging

F5a fibrosarcomas were grown on the legs of 6–8-week-old C3H mice (HSD, Indianapolis, IN) immobilized with a partial circumference vinyl polysiloxane cast (GC Dental Products, Kasugai, Japan) (28). For Fig. 4, OX063 was injected IV 0.56 mmol/kg followed by infusion at 0.63 mmol/kg/hr. In Fig. 5, after each R_{1e}/R_{2e} image pair additional 0.21 mmol/kg OX063 was injected, and infusion was increased by 0.35 mmol/kg /hour, to a maximum of

3.85 mmol/kg /hour. This was performed on three animals with consistent results. Tumor was defined by T_2 enhancement in RARE MRI registered with EPR images (29).

Animal experiments followed USPHS policy, and were approved by the Institutional Animal Care and Use Committee.

Results

In vitro studies show reduction of R_{1e} sensitivity to confounding [trityl] relaxation by nearly an order of magnitude relative to that of R_{2e}

We performed studies *in vitro* by using the OX063 spin probe, as described in Methods (15,30,31). Sodium chloride concentration affects the relaxation times (8). Thus, normal saline (145 mM NaCl) resembling animal condition, was used as solvent (1). Temperature, was kept at 37°C, as in rodents and humans (32). These conditions affected the relaxation times and made them substantially different from the measurements on the same spin probe dissolved in water and performed at room temperature; see for example (33). In saline sodium ions allow the tri-acid OX063, whose charge is -3 at physiologic pH, to approach more closely to each other than in water, increasing [trityl] dependent transverse self-relaxation. The dependence of OX063 relaxation rates on pO_2 is given in Figure 3a. The experimental data were corrected for the effect of spin probe concentration, referred to as [trityl] by applying linear relation between [trityl] and relaxation rate (Fig. 3b). It should be noted that relaxation rates of spin probe in water show weaker and non-linear dependence on [trityl] (data not shown). The reasons for that are under investigation. There was no significant difference between the slopes of the linear dependences of R_{1e} and R_{2e} on pO_2 . However, there was a dramatic difference in the slopes of the dependences of R_{1e} and R_{2e} on spin probe concentration, referred to as [trityl] (Fig. 3b). R_{2e} vs [trityl] had nearly five times greater slope than did R_{1e} .

The quantitative dependence of R_{2e} on [trityl] is much weaker than on pO_2 or O_2 concentration, referred to as $[O_2]$. At 37 °C, $[O_2]$ in saline solution is 219 μM at 159 torr or $\sim 1.4 \mu\text{M}/\text{torr}$. Thus, the sensitivity of trityl R_{2e} to $[O_2]$ is $\sim 6.3 \cdot 10^6 \text{ s}^{-1}/\text{mM}$, but only $0.165 \cdot 10^6 \text{ s}^{-1}/\text{mM}$ for [trityl].

The results of R_{1e} imaging and relaxation measurements of phantoms with 0% and 9.3% O_2 (71 torr pO_2 at 37 °C and atmospheric pressure) are summarized in Table 3. These $[O_2]$ bracket relevant values from pO_2 studies of hypoxia in animals (15,34). The relaxation times determined under non-imaging conditions are given in the footnotes of the table. No significant difference between average relaxation times determined under imaging and non-imaging conditions was found.

Residual dependence of R_{1e} on [trityl] is likely due to spectral diffusion, the interaction of excited spins with the other spins whose EPR frequencies are beyond the excitation bandwidth (20). Such spins may be from trityl molecules containing ^{13}C (1.109% natural abundance) producing hyperfine lines split up to 12 G from the central line, (35) considerably beyond the excitation bandwidth of the pulse sequence. The results of R_{2e} measurements using ESE are given in the table for comparison. To estimate errors, the

standard deviation of the relaxation times was estimated for homogeneous phantom voxels, excluding regions with edge artifacts. The R_{2e} image had a standard deviation smaller than that of the R_{1e} imaging method. However, for 0% O_2 the standard deviation of the R_{1e} image approached that of the R_{2e} image.

R_{1e} in the tumor of a live animal shows far more freedom from [trityl] relaxation

For a demonstration of the robustness of R_{1e} imaging on a live animal tumor (Fig. 4b), we compared the IRESE image slice with the same slice from the R_{2e} image (Fig. 4a), obtained from a two-pulse ESE image on the same animal 10 minutes later. The brighter, richly colored areas in both of the images are well oxygenated, whereas the darker, more intensely blue areas are hypoxic. The tumor outline from a registered T_2 -weighted MRI is shown in both the images as red contours. The outlines and general oxygenation patterns are very similar. However, absolute voxel pO_2 values differ considerably. Figure 4c presents the [trityl] image obtained with two-pulse ESE. Figures 4d and 4e are histograms of the R_{2e} and R_{1e} relaxation rates, respectively. The red-colored histograms are from the voxels enclosed by the red tumor contours in Figs. 4a–c. The blue histogram bars are from the leg tissue outside the tumor contours. They are added to the tumor histogram bars so that the ultimate height of the blue plus red histogram bars represents the total number of image voxels with the indicated relaxation rate.

The mode of the overall R_{1e} distribution from the tumor shown in Fig. 4e is nearly $0.35 \cdot 10^6 \text{ s}^{-1}$ smaller than that from the R_{2e} image. In the distributions of the R_{1e} and R_{2e} , there are two components with different modes and widths – the tumor and the residual leg area. The sharper component with the lower mode, localized primarily in the tumor area, is more clearly distinguished in the R_{1e} image. That component is associated with the narrower distribution of relaxation rates expected in the hypoxic tumor area and shows the improved performance of R_{1e} imaging. The slowest R_{1e} observed in the animal experiments (Fig. 4e) are very close to the rates found in deoxygenated phantoms. This is expected because tumors are frequently hypoxic. R_{2e} rates, however, are $\sim 0.35 \cdot 10^6 \text{ s}^{-1}$ higher than R_{1e} rates (Fig. 4f). Because the relaxation rates due to different mechanisms are additive, the shift of the distribution toward higher values indicates that R_{2e} images are more susceptible to O_2 -independent relaxation than is R_{1e} . At room temperature and at a negligible [trityl] the R_{2e} and R_{1e} are similar.

Ultimately, the advantage of R_{1e} -based pO_2 imaging over R_{2e} -based pO_2 imaging lies in its reduced susceptibility to confounding variation from [trityl]-induced relaxation. We demonstrated this by artificially increasing [trityl] by increasing the rate of trityl infusion to an animal and assessing the changes in the relaxation rates in selected regions. Although the local tissue oxygenation in subvolumes of tumors is known to vary (36,37), we assumed the average tissue oxygenation during the experiment to be constant. We justify this assumption below based on the results. In the absence of changes in oxygenation all changes in the relaxation rates should be from [trityl] relaxation effect. As a surrogate for the local [trityl], we used the voxel signal intensity obtained from R_{2e} images normalized to the intensity of voxels in a 1 mM phantom. The voxel signal intensity is R_{2e} -independent because the spin echo amplitude was extrapolated to $\tau=0$. In Figure 5, the change in relaxation rates was

imaged by alternating ESE and IRESE images. The [trityl], estimated from the ESE images, in animal tissues was stabilized prior to imaging by comparison of consecutive image intensities. Two regions of the image, one directly in the tumor volume and the other just outside the tumor volume in a well-perfused region, were compared for each image type. The regions consisted of a cube of $3 \times 3 \times 3 = 27$ voxels, as seen in the leftmost image which shows a sagittal slice including the regions. The R_{2e} and R_{1e} are plotted to the right of the image slice from each region. The [trityl] dependence coefficients of R_{2e} and R_{1e} are indicated along with their uncertainties determined from the scatter of values about the regression lines. The R_{2e} values, for each location, depend strongly on the apparent [trityl] while the R_{1e} values are independent of [trityl] to within the value uncertainties shown. The effect of [trityl] on R_{2e} is considerably stronger than the effect of cycling hypoxia (36,37) and, more importantly is observed not only in tumor but in all anatomic areas.

Discussion

This work demonstrates that R_{1e} images have nearly an order of magnitude reduced sensitivity to self-relaxation *in vivo* and, thus, higher accuracy. The precision of R_{1e} and R_{2e} images is very similar, especially at low $[O_2]$. Figure 5 shows that R_{2e} does indeed depend on [trityl] *in vivo*. The trend is clearly visible because the range of [trityl] in Figure 5b is far larger than typically found in *in vivo* images. The slopes of R_{2e} [trityl] dependences in Fig. 5 ranging from $0.2 \cdot 10^6$ to $0.9 \cdot 10^6 \text{ s}^{-1}/\text{mM}$ are considerably stronger than that found in the phantoms ($0.165 \cdot 10^6 \text{ s}^{-1}/\text{mM}$). In part, this may be due to our underestimation of the real spin probe concentration. The tri-acid spin probe cannot penetrate the cell membrane at physiologic pH (16). Its extracellular distribution volume can be as small as 30% of the tissue volume (38) increasing the actual concentration by a factor of three relative to that based on voxel intensity. The [trityl] dependence of R_{1e} is five times smaller in phantoms and is undetectable *in vivo*, Fig. 5, areas [1] and [2]. The pO_2 , inferred from the R_{1e} images in each voxel are, to within the uncertainty, accurate and are the absolute measurements of tissue or tumor oxygenation.

As noted above, virtually all *in vivo* EPR O_2 images have exploited sensitivity of R_{2e} to local pO_2 , except for one qualitative study (18). The present study demonstrates, for the first time, pulse EPR O_2 imaging in live animals that is sensitive to the spin probe electron R_{1e} . The long relaxation times of trityls and the O_2 -induced changes in R_{1e} are much more favorable than with the nitroxides used in the past as an infusible spin probe for O_2 imaging *in vivo* (39,40). R_{1e} -based O_2 imaging is superior to R_{2e} or R_{2e}^* imaging modalities because of the reduced sensitivity to [trityl]. The [trityl] *in vivo* is difficult to control and, given the unknown volume in each voxel occupied by the extracellular trityl spin probe, is difficult to determine accurately. The accuracy of R_{1e} O_2 images is thus improved by virtually eliminating sensitivity to trityl concentration.

Conclusions

R_{1e} EPR O_2 imaging with trityl spin probes is feasible and has the same precision as R_{2e} imaging. The absolute accuracy of this method is superior to R_{2e} imaging because of the smaller confounding effect of environmental parameters other than O_2 on R_{1e} . Therefore,

R_{1e} EPR imaging should be considered as a primary method for oxymetry. Ten-minute images of a 1 mM hypoxic sample provide 1 torr pO_2 resolution with 1–1.5 mm spatial resolution (14,19).

The improved accuracy of the O_2 images, presented here, should further enhance animal studies of tissue and tumor oxygenation. The low radiofrequency at which these studies have been undertaken and the large animal tumors already studied with R_{2e} pO_2 images (29) argue for the distinct possibility for measurements in human tumors. pO_2 images can direct therapy of cancers with radiation. The enhanced accuracy of R_{1e} pO_2 imaging shown here argues strongly for this technique to be incorporated in future animal and perhaps human images.

Acknowledgments

Work was supported by NIH grants P41EB002034 and CA98575.

References

1. Longo, DL.; Fauci, AS.; Kasper, DL.; Hauser, SL.; Jameson, JL.; Loscalzo, J., editors. *Harrison's Principles of Internal Medicine*. 18 ed.. Vol. 1. New York, NY: McGraw Hill; 2011. p. 3610
2. Tatum JL, Kelloff GJ, Gillies RJ, Arbeit JM, Brown JM, Chao KSC, Chapman JD, Eckelman WC, Fyles AW, Giaccia AJ, Hill RP, Koch CJ, Krishna MC, Krohn KA, Lewis JS, Mason RP, Melillo G, Padhani AR, Powis G, Rajendran JG, Reba R, Robinson SP, Semenza GL, Swartz HM, Vaupel P, Yang D, Croft B, Hoffman J, Liu G, Stone H, Sullivan D. Hypoxia: Importance in tumor biology, noninvasive measurement by imaging, and value of its measurement in the management of cancer therapy. *Int J Radiat Biol*. 2006; 82(10):699–757. [PubMed: 17118889]
3. Brizel DM, Sibley GS, Prosnitz LR, Scher RL, Dewhirst MW. Tumor hypoxia adversely affects the prognosis of carcinoma of the head and neck. *Int J Radiat Oncol Biol Phys*. 1997; 38(2):285–289. [PubMed: 9226314]
4. Semenza GL. Hypoxia-inducible factor 1: master regulator of O_2 homeostasis. *Curr Opin Genet Dev*. 1998; 8(5):588–594. [PubMed: 9794818]
5. Semenza GL. HIF-1, O(2), and the 3 PHDs: how animal cells signal hypoxia to the nucleus. *Cell*. 2001; 107(1):1–3. [PubMed: 11595178]
6. Elas M, Hleihel D, Barth ED, Haney CR, Ahn KH, Pelizzari CA, Epel B, Weichselbaum RR, Halpern HJ. Where it's at really matters: in situ in vivo vascular endothelial growth factor spatially correlates with electron paramagnetic resonance pO_2 images in tumors of living mice. *Mol Imaging Biol*. 2011; 13(6):1107–1113. [PubMed: 20960236]
7. Molin, YN.; Salikhov, KM.; Zamaraev, KI. *Spin Exchange: Principles and Applications in Chemistry and Biology*. Goldanskii, VI.; Gomer, R.; Schafer, FP.; Toennies, JP., editors. Berlin: Springer-Verlag; 1980. p. 242
8. Ardenkjaer-Larsen JH, Laursen I, Leunbach I, Ehnholm G, Wistrand LG, Petersson JS, Golman K. EPR and DNP properties of certain novel single electron contrast agents intended for oximetric imaging. *J Magn Reson*. 1998; 133(1):1–12. [PubMed: 9654463]
9. Abragam, A. *Principles of Nuclear Magnetism*. Oxford: Oxford University; 1961.
10. Popp CA, Hyde JS. Effects of Oxygen on Electron-Paramagnetic-Resonance of Nitroxide Spin-Label Probes of Model Membranes. *J Magn Reson*. 1981; 43(2):249–258.
11. Subczynski WK, Hyde JS. The Diffusion-Concentration Product of Oxygen in Lipid Bilayers Using the Spin-Label T1 Method. *Biochim Biophys Acta*. 1981; 643(2):283–291. [PubMed: 6261814]
12. Halpern HJ, Yu C, Peric M, Barth E, Grdina DJ, Teicher BA. Oxymetry Deep in Tissues with Low-Frequency Electron-Paramagnetic-Resonance. *Proc Natl Acad Sci USA*. 1994; 91(26): 13047–13051. [PubMed: 7809170]

13. Subramanian S, Devasahayam N, Murugesan R, Yamada K, Cook J, Taube A, Mitchell JB, Lohman JA, Krishna MC. Single-point (constant-time) imaging in radiofrequency Fourier transform electron paramagnetic resonance. *Magn Reson Med*. 2002; 48(2):370–379. [PubMed: 12210946]
14. Epel B, Sundramoorthy SV, Mailer C, Halpern HJ. A versatile high speed 250-MHz pulse imager for biomedical applications. *Conc Magn Reson B*. 2008; 33B(3):163–176.
15. Elas M, Williams BB, Parasca A, Mailer C, Pelizzari CA, Lewis MA, River JN, Karczmar GS, Barth ED, Halpern HJ. Quantitative tumor oxymetric images from 4D electron paramagnetic resonance imaging (EPRI): Methodology and comparison with blood oxygen level-dependent (BOLD) MRI. *Magnet Reson Med*. 2003; 49(4):682–691.
16. Williams BB, al Hallaq H, Chandramouli GV, Barth ED, Rivers JN, Lewis M, Galtsev VE, Karczmar GS, Halpern HJ. Imaging spin probe distribution in the tumor of a living mouse with 250 MHz EPR: correlation with BOLD MRI. *Magn Reson Med*. 2002; 47(4):634–638. [PubMed: 11948723]
17. Kusumi A, Subczynski WK, Hyde JS. Oxygen-Transport Parameter in Membranes as Deduced by Saturation Recovery Measurements of Spin-Lattice Relaxation-Times of Spin Labels. *P Natl Acad Sci-Biol*. 1982; 79(6):1854–1858.
18. Hama Y, Matsumoto KI, Murugesan R, Subramanian S, Devasahayam N, Koscielniak JW, Hyodo F, Cook JA, Mitchell JB, Krishna MC. Continuous wave EPR oximetric imaging at 300 MHz using Radiofrequency power saturation effects. *Antioxidants & Redox Signaling*. 2007; 9(10): 1709–1716. [PubMed: 17696765]
19. Epel B, Sundramoorthy SV, Barth ED, Mailer C, Halpern HJ. Comparison of 250 MHz electron spin echo and continuous wave oxygen EPR imaging methods for in vivo applications. *Medical Physics*. 2011; 38(4):2045–2052. [PubMed: 21626937]
20. Schweiger, A.; Jeschke, G. *Principles of Pulse Electron Paramagnetic Resonance*. Oxford University Press; 2001.
21. Mailer C, Sundramoorthy SV, Pelizzari CA, Halpern HJ. Spin echo spectroscopic electron paramagnetic resonance imaging. *Magnet Reson Med*. 2006; 55(4):904–912.
22. Sundramoorthy SV, Epel B, Mailer C, Halpern HJ. A Passive Dual-Circulator Based Transmit/Receive Switch for Use with Reflection Resonators in Pulse Electron Paramagnetic Resonance. *Conc Magn Reson B*. 2009; 35B(3):133–138.
23. Quine RW, Tseytlin M, Eaton SS, Eaton GR. A Very Fast Switched Attenuator Circuit for Microwave and R.F. Applications. *Concepts Magn Reson Part B Magn Reson Eng*. 2010; 37B(2): 39–44. [PubMed: 21546999]
24. Epel B, Gromov I, Stoll S, Schweiger A, Goldfarb D. Spectrometer manager: A versatile control software for pulse EPR spectrometers. *Conc Magn Reson B*. 2005; 26B(1):36–45.
25. Ahn KH, Halpern HJ. Simulation of 4D spectral-spatial EPR images. *J Magn Reson*. 2007; 187(1): 1–9. [PubMed: 17434772]
26. Ahn KH, Halpern HJ. Spatially uniform sampling in 4-D EPR spectral-spatial imaging. *J Magn Reson*. 2007; 185(1):152–158. [PubMed: 17197215]
27. Ahn KH, Halpern HJ. Comparison of local and global angular interpolation applied to spectral-spatial EPR image reconstruction. *Med Phys*. 2007; 34(3):1047–1052. [PubMed: 17441251]
28. Haney CR, Fan X, Parasca AD, Karczmar GS, Halpern HJ, Pelizzari CA. Immobilization using dental material casts facilitates accurate serial and multimodality small animal imaging. *Conc Magn Reson B*. 2008; 33B(2):138–144.
29. Epel B, Haney CR, Hleihel D, Wardrip C, Barth ED, Halpern HJ. Electron paramagnetic resonance oxygen imaging of a rabbit tumor using localized spin probe delivery. *Medical Physics*. 2010; 37(6):2553–2559. [PubMed: 20632567]
30. Matsumoto K, Subramanian S, Devasahayam N, Aravalluvan T, Murugesan R, Cook JA, Mitchell JB, Krishna MC. Electron paramagnetic resonance imaging of tumor hypoxia: enhanced spatial and temporal resolution for in vivo pO₂ determination. *Magn Reson Med*. 2006; 55(5):1157–1163. [PubMed: 16596636]

31. Elas M, Ahn KH, Parasca A, Barth ED, Lee D, Haney C, Halpern HJ. Electron paramagnetic resonance oxygen images correlate spatially and quantitatively with oxylyte oxygen measurements. *Clinical Cancer Research*. 2006; 12(14):4209–4217. [PubMed: 16857793]
32. Krogh, A. *The Comparative Physiology of Respiratory Mechanisms*. Philadelphia: University of Philadelphia Press; 1941.
33. Owenius R, Eaton GR, Eaton SS. Frequency (250 MHz to 9.2 GHz) and viscosity dependence of electron spin relaxation of triarylmethyl radicals at room temperature. *J Magn Reson*. 2005; 172(1):168–175. [PubMed: 15589420]
34. Elas M, Bell R, Hleihel D, Barth ED, Mcfaul C, Haney CR, Bielanska J, Pustelny K, Ahn KH, Pelizzari CA, Kocherginsky M, Halpern HJ. Electron paramagnetic resonance oxygen image hypoxic fraction plus radiation dose strongly correlates with tumor cure in FSA fibrosarcomas. *International Journal of Radiation Oncology Biology Physics*. 2008; 71(2):542–549.
35. Bowman MK, Mailer C, Halpern HJ. The solution conformation of triarylmethyl radicals. *J Magn Reson*. 2005; 172(2):254–267. [PubMed: 15649753]
36. Yasui H, Matsumoto S, Devasahayam N, Munasinghe JP, Choudhuri R, Saito K, Subramanian S, Mitchell JB, Krishna MC. Low-Field Magnetic Resonance Imaging to Visualize Chronic and Cycling Hypoxia in Tumor-Bearing Mice. *Cancer Research*. 2010; 70(16):6427–6436. [PubMed: 20647318]
37. Matsumoto S, Yasui H, Mitchell JB, Krishna MC. Imaging Cycling Tumor Hypoxia. *Cancer Research*. 2010; 70(24):10019–10023. [PubMed: 21159626]
38. Ganong, WF. *Review of Medical Physiology*. San Mateo, CA: Appleton & Lange; 1987.
39. Halpern HJ, Yu C, Peric M, Barth E, Grdina DJ, Teicher BA. Oxymetry deep in tissues with low-frequency electron paramagnetic resonance. *Proc Natl Acad Sci USA*. 1994; 91(26):13047–13051. [PubMed: 7809170]
40. Velan SS, Spencer RG, Zweier JL, Kuppusamy P. Electron paramagnetic resonance oxygen mapping (EPRM): direct visualization of oxygen concentration in tissue. *Magn Reson Med*. 2000; 43(6):804–809. [PubMed: 10861874]

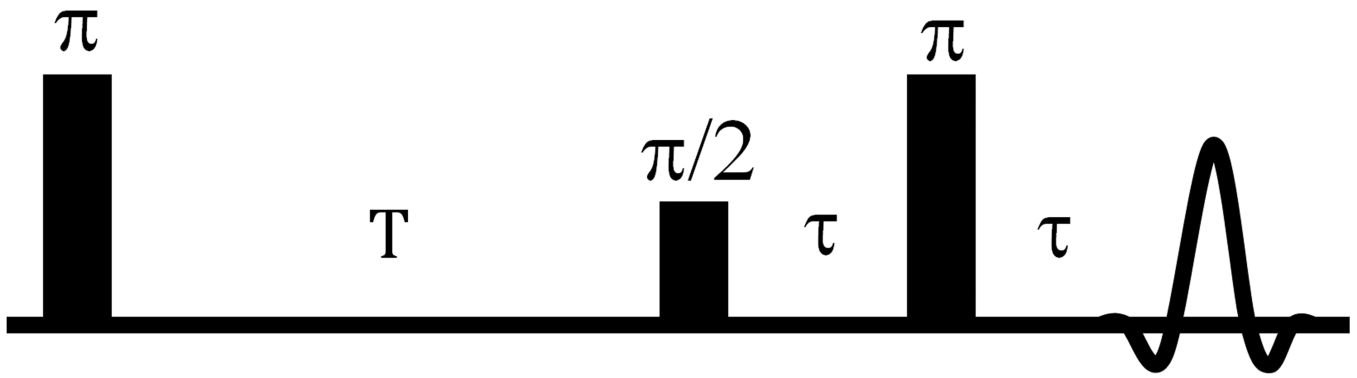


Figure 1.
IRESE pulse sequence for R_{1e} imaging.

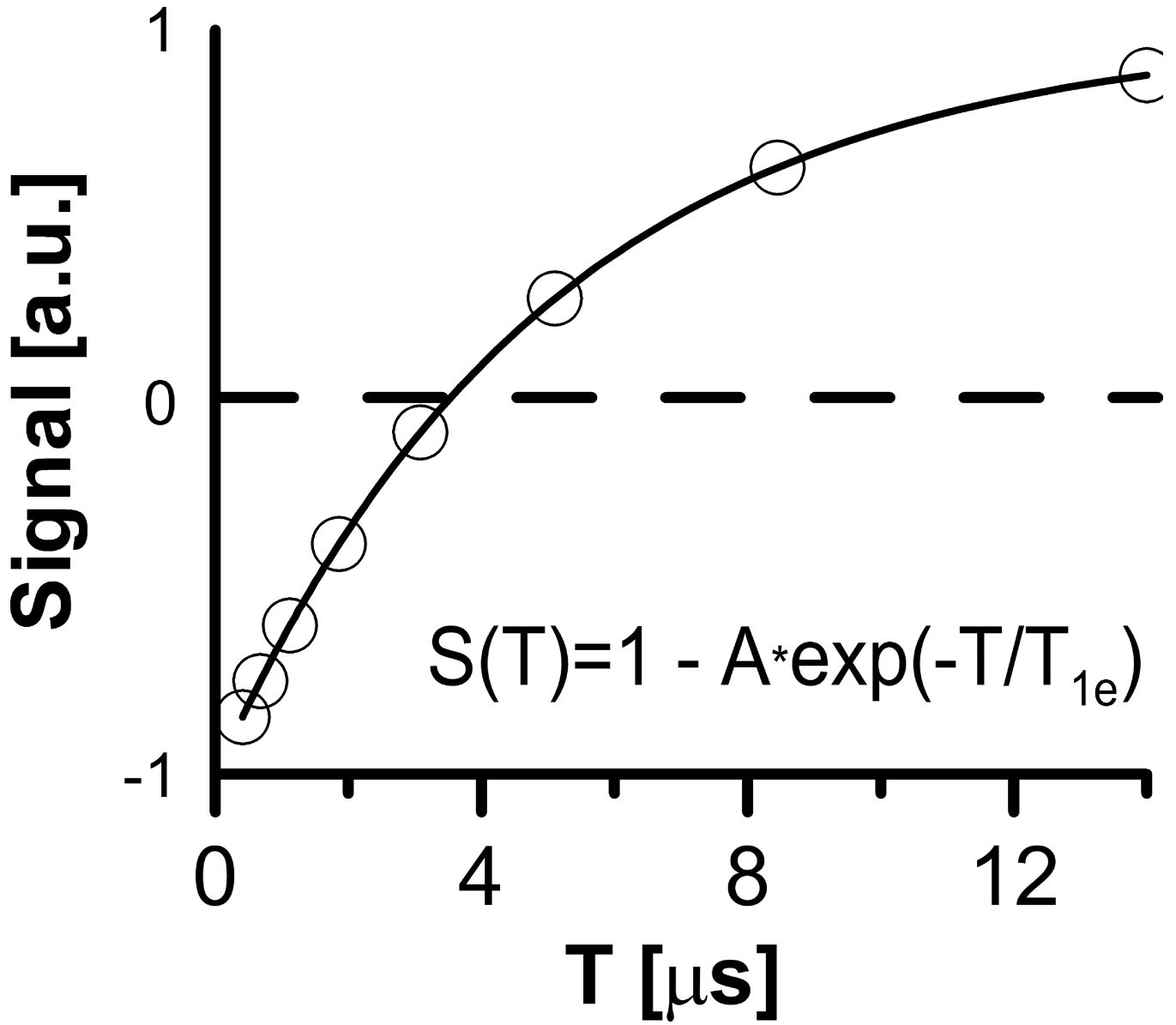


Figure 2. Simulation of a single voxel's signal amplitude dependence on T in IRESE sequence. $T_{1e} = 5 \mu s$ was used.

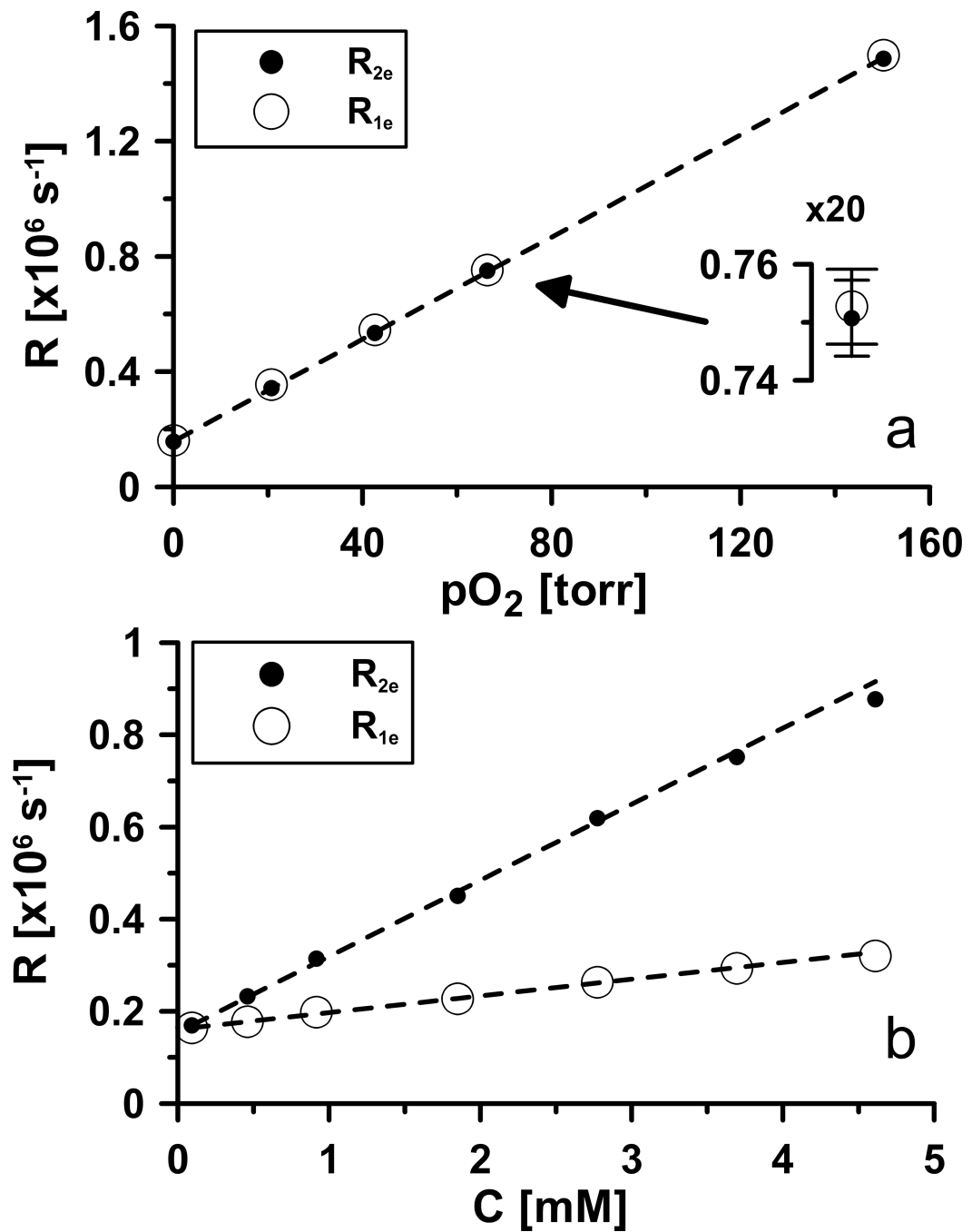


Figure 3.

Relaxation rates of OX063 dissolved in saline at 37°C.

a. [trityl] corrected dependence (concentration independent) of relaxation rates on $p\text{O}_2$. The data were obtained using 0.46 mM sample. The relaxation rates were then extrapolated to zero [trityl] by subtracting $0.46\text{mM} \cdot 0.165 \cdot 10^6 \text{ s}^{-1}/\text{mM} = 76 \cdot 10^3 \text{ s}^{-1}$ for R_{2e} , and $0.46\text{mM} \cdot 36.3 \cdot 10^3 \text{ s}^{-1}/\text{mM} = 17 \cdot 10^3 \text{ s}^{-1}$ for R_{1e} . Best fit: $R_{1e} = 8.9 \cdot 10^3 \text{ s}^{-1}/\text{torr} \cdot p\text{O}_2 + 1.6 \cdot 10^5 \text{ s}^{-1}$; $R_{2e} = 8.9 \cdot 10^3 \text{ s}^{-1}/\text{torr} \cdot p\text{O}_2 + 1.6 \cdot 10^5 \text{ s}^{-1}$.

b. [trityl] dependences of relaxation rates R_{1e} and R_{2e} . Best fit: $R_{1e} = 36.3 \cdot 10^3 \text{ s}^{-1}/\text{mM} \cdot [\text{trityl}] + 0.16 \cdot 10^5 \text{ s}^{-1}$; $R_{2e} = 0.165 \cdot 10^6 \text{ s}^{-1}/\text{mM} [\text{trityl}] + 0.16 \cdot 10^5 \text{ s}^{-1}$.
The 95% confidence intervals for fit parameters are: $\pm 1 \cdot 10^4 \text{ s}^{-1}$ for offsets, $\pm 1.2 \cdot 10^2 \text{ s}^{-1}/\text{torr}$ for O_2 and $\pm 7 \cdot 10^3 \text{ s}^{-1}/\text{mM}$ for concentration proportionality coefficients.

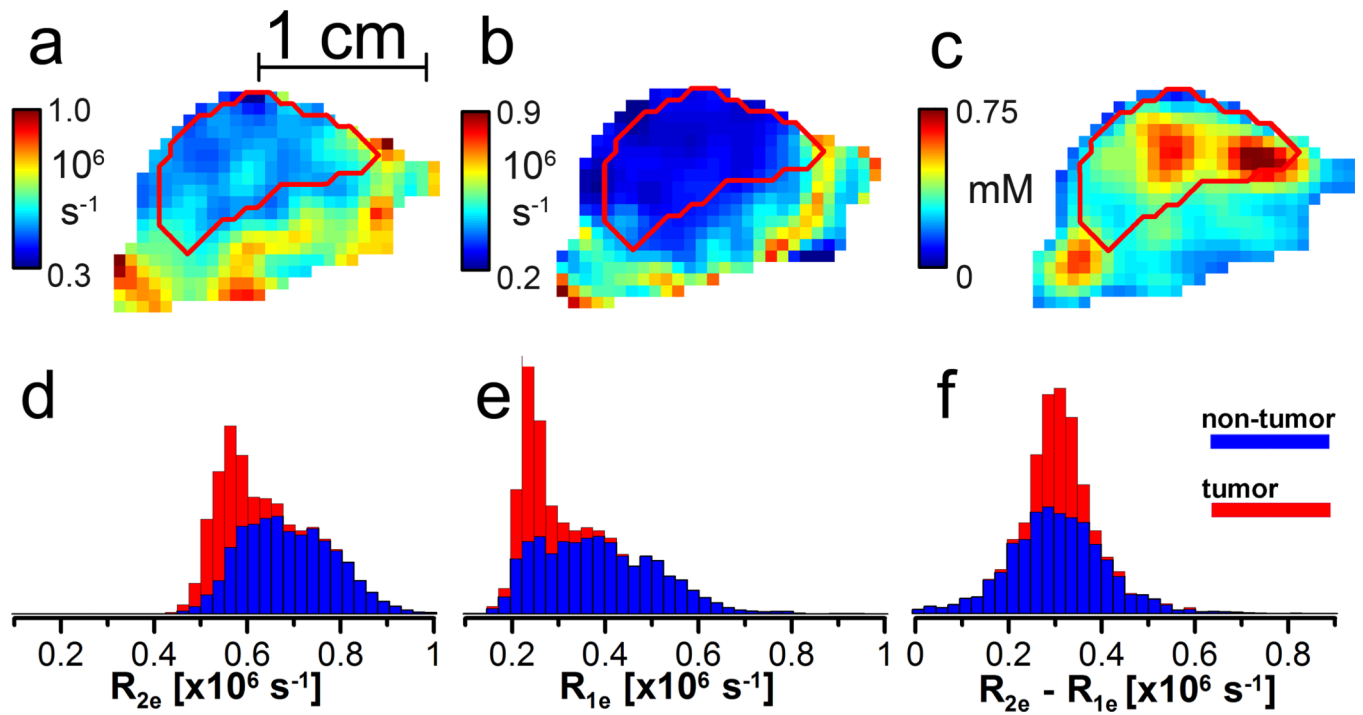


Figure 4.

a–c: sagittal slice (0.7 mm) of a mouse leg bearing a tumor. a. R_{2e} image from ESE; b. R_{1e} image from IRESE; and c. [trityl] image from ESE. The tumor contour is obtained from a registered MRI. d–f: stacked histograms of d. R_{2e} ; e. R_{1e} ; and f. the difference between R_{1e} and R_{2e} .

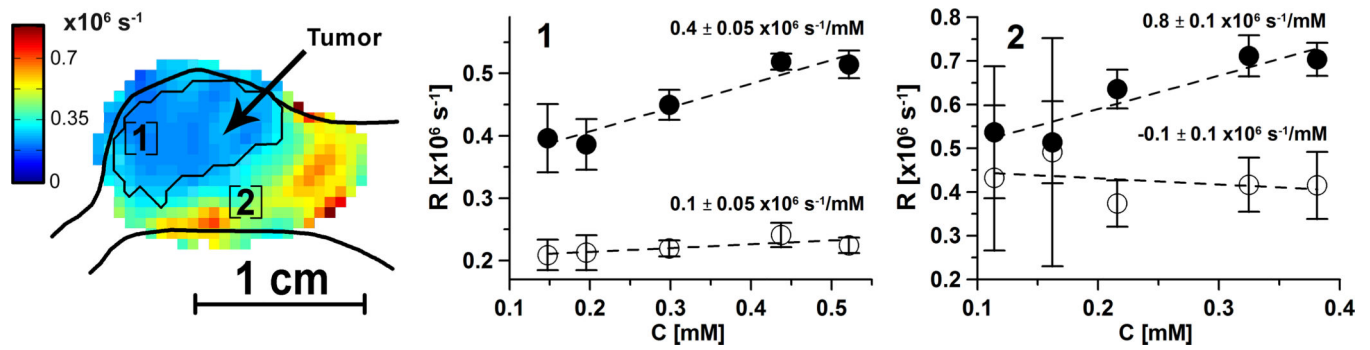


Figure 5.

R_{1e} (○) and R_{2e} (●) in a mouse vs [trityl] as spin probe is infused at different rates. [trityl] is obtained by normalization of animal signal intensity in each voxel on the voxel intensity of phantom with 1mM concentration. A sagittal slice of R_{1e} image of the tumor-bearing leg is shown on the left. Leg profile and tumor contour are obtained from registered T_2 -weighted MRI. R_{1e} and R_{2e} [trityl] dependences for two areas [1] and [2] obtained by averaging voxels in $\sim 8 \text{ mm}^3$ cube (27 voxels) are shown. Error bars are the R_{1e} and R_{2e} standard deviations. Area 1 is located in the tumor, and area 2 is in the muscle. The slopes of [trityl] dependence and 50% confidence intervals are given in the plots.

Table 1

Pulse sequences and imaging protocols.

Protocol	Description
Non-imaging two-pulse ESE	$\pi/2$ - τ - π - τ -echo; 35 ns $\pi/2$ and π RF pulses; 80 τ 's logarithmically spaced between 630 ns and 14 μ s; 16-step phase cycling; 70 μ s repetition time; echo is integrated; τ s are measured in random order.
Non-imaging IRESE	π -T- $\pi/2$ - τ - π - τ -echo; 35 ns $\pi/2$ and π RF pulses; τ = 630 ns; 16-step phase cycling for detection sequence; 80 Ts are spaced logarithmically between 0.5 μ s and 32 μ s; 80 μ s repetition time; echo is integrated; Ts are measured in random order.
Two-pulse ESE imaging	$\pi/2$ - τ - π - τ -echo; 35 ns $\pi/2$ and π RF pulses; time trace 1500 points with 4 ns dwell time; 16-step phase cycling, 37472 acquisitions per τ , including phase cycling; 5 τ s are spaced logarithmically between 0.63 μ s and 2.4 μ s; T_{R}^{LF} = 10.37 μ s; $ G $ =15 mT/m; imaging time 10 minutes.
IRESE imaging	π -T- $\pi/2$ - τ - π - τ -echo; 35 ns $\pi/2$ and π RF pulses; time trace 1500 points with 4 ns dwell time; τ = 630 ns; 16-step phase cycling applied only for detection sequence, 9600 acquisitions per T, including phase cycling; 8 Ts are spaced logarithmically between 0.41 μ s and 14 μ s; T_{R}^{LF} = 25 μ s; $ G $ =15 mT/m; imaging time 10 minutes.

Table 2

Parameters of pulse sequences

	Pulse length	RF power [W]	Bandwidth [MHz]	Transmitted Average Power [W]
2pESE (T_{2e})	35 ns, $\pi/2$ and π	39.6 ($\pi/2$), 158.5 (π)	8.7	0.57
IRESE (T_{1e})	35 ns, $\pi/2$ and π	39.6 ($\pi/2$), 158.5 (π)	8.7	0.42

Precision of images estimated as a standard deviation of relaxation times in an image of homogeneous phantom. Images are obtained in 10 minutes on phantom containing 1 mM OX063 dissolved in normal saline at 37°C. No [trityl] correction is applied.

Table 3

Pulse Sequence	0% pO ₂		9.3% pO ₂	
	Average T _{2e} or T _{1e} [μs]	Standard deviation of T _{2e} or T _{1e} [μs]	Average T _{2e} or T _{1e} [μs]	Standard deviation of T _{2e} or T _{1e} [μs]
TR measurements (T _{2e} and R _{2e})				
2pESE	3.1	0.2	1.25	0.07
				46*
SLR measurements (T _{1e} and R _{1e})				
IRESE	5.0	0.3	1.31	0.15
				90*

Non-imaging relaxation times: for 0% O₂ sample T_{2e} = 2.99 μs (two-pulse ESE), T_{1e} = 4.82 μs (IRESE); for 9.3% O₂ sample T_{2e} = 1.24 μs (two-pulse ESE), T_{1e} = 1.33 μs (IRESE).

* 7.9·10³ s⁻¹ corresponds to 0.9 torr; 46·10³ s⁻¹ corresponds to 5 torr; 90·10³ s⁻¹ corresponds to 10 torr.